Springer

KSME

Journal of Mechanical Science and Technology 33 (5) (2019) 2289~2305
www.springerlink.com/content/1738-494x(Print)/1976-3824(Online)
DOI 10.1007/s12206-019-0430-y

Buckling analysis of thin-walled box beams under arbitrary loads with general boundary conditions using higher-order beam theory †

Do-Min Kim[1], Soomin Choi[2], Gang-Won Jang[3] and Yoon Young Kim[1,*]

[1]*WCU Multiscale Mechanical Design Division, School of Mechanical and Aerospace Engineering, Seoul National University, Seoul 08826, Korea*
[2]*School of Mechanical and Aerospace Engineering, Seoul National University, Seoul 08826, Korea*
[3]*School of Mechanical and Aerospace Engineering, Sejong University, Seoul 05006, Korea*

(Manuscript Received November 13, 2018; Revised January 18, 2019; Accepted February 1, 2019)

Abstract

When a higher-order or generalized beam theory is used for the buckling analysis of thin-walled beams, the analysis accuracy critically depends on the number and shapes of the cross-sectional modes associated with warping and distortion. In the study, we propose to use the hierarchically-derived cross-sectional modes consistent with the higher-order beam theory for the analysis of pre-buckling stress and buckling load. The proposed formulation is applicable to any box beams subjected to arbitrary loads and general boundary conditions. We demonstrate the effectiveness of the proposed method by performing buckling analyses for axial, bending, torsional, and general loadings. Length-to-height ratios of the beams are also varied from 1 to 100. If up to fifty cross-sectional and rigid-body modes are employed, the calculated buckling loads are found to match favorably those predicted by the shell finite element analysis. In that a unified buckling analysis under general loads is developed for box beams, the present study is expected to contribute towards new possibilities for the efficient buckling analysis of more general box beam structures involving several joints.

Keywords: Buckling behavior; Cross-sectional deformation; Global/local buckling mode; Higher-order beam theory (HoBT); Thin-walled box beam

1. Introduction

In contrast to solid beams, thin-walled beams involve global and local buckling modes when they buckle. Local modes involve localized cross-sectional deformations at several points along the beam axis. Specifically, these modes stem from the buckling of the wall plates of a thin-walled beam. A dominant deformation pattern in local modes is distortion, i.e., a sectional in-plane deformation. Cross-sectional deformations of box beams are developed even in global buckling, and thus the classical Euler or Timoshenko beam theories cannot accurately predict the buckling loads and modes of thin-walled beams. The accuracy by these classical beam theories becomes worse especially when the box beams are not long. In the case when a box beam is shorter than a certain length, a local buckling mode appears as the primary buckling mode because the buckling of wall plates forming a box beam is dominant. Prior to proposing a method to accurately predict the buckling phenomenon of thin-walled box beams with a higher-order beam theory, we will review related extant investigations to validate the need for an alternative approach as discussed in the study.

If a thin-walled box beam is viewed as a plate structure, a discrete plate model can be employed as in Refs. [1-3]. In the aforementioned studies, a thin-walled beam is considered as an assembly of thin plates having various boundary conditions. Typically, different boundary conditions are considered based on loading and bonding conditions between the wall plates of a box beam. Because they used a plate theory, the analysis was more complicated than that using a (higher-order) beam theory. The finite strip methods were proposed by Refs. [4-8], in which the distortional deformations of the beam section were taken into account. Methods mainly considering warping were also proposed [9-12]. In these methods, nodal displacements at each corner were used as the beam degrees of freedom (DOFs) to describe warping deformation.

The aforementioned methods utilized plate/shell theories although there were alternative methods based on advanced beam theories such as generalized or higher-order beam theories. Vlasov's theory [13] incorporating a distortional degree of freedom was expanded to perform buckling analyses of thin-walled beams by using the generalized beam theory (GBT) [14-19]. It was shown that the inclusion of the distortional and warping degrees of freedom in addition to the classical beam DOFs accurately predicts the buckling phenomenon of thin-walled beams [16]. Genoese et al. [20] and Garcea

*Corresponding author. Tel.: +82 2 880 7154, Fax.: +82 2 872 5431
E-mail address: yykim@snu.ac.kr
† Recommended by Associate Editor Guangyong Sun

et al. [21] proposed the generalized eigenvector method focused on the derivation of semi-analytic solutions. The method also used sectional DOFs to accurately describe buckling behavior although the cross-sectional deformations of a box beam were derived based on three-dimensional continuum analysis in contrast to other advanced beam theories. Alternatively, a higher order beam model was developed based on numerically derived sectional DOFs to capture global/local buckling modes accurately [22, 23]. One-dimensional beam formulations were also used to predict the buckling behavior of thin-walled composite beams [24-26]. Meanwhile, non-linear beam formulations stemming from Abramowicz [27] and Kecman [28] were developed for the simplified analysis and design of thin-walled crashworthiness structures [29-32].

Here, we aim to employ another advanced beam theory called higher-order beam theory (HoBT) for buckling analysis. The HoBT has been developed for static and dynamic analyses of box beams [33-39]. The theory was also shown to be effective in dealing with box beam joint problems [37, 38]. Because theoretical joint matching conditions appear to be available only for the HoBT, the buckling analysis of multiply-connected box beam structures should be based on the HoBT. In this respect, the present buckling analysis based on the HoBT must be developed before the analysis of multiply-connected box beams. The developed analysis method should be useful for any thin-walled box beams under general boundary conditions and arbitrary loadings.

In HoBT, warping and distortional DOFs are considered in addition to the classical six DOFs. To derive cross-sectional shape functions for the buckling analysis, we employ the method presented in Ref. [38]. Specifically, we use the hierarchical and systematic method to derive the cross-sectional deformation mode shapes related to warping and distortion. If the hierarchical method in Ref. [38] is used, one can adjust solution accuracy by selecting different numbers of the cross-sectional deformation modes. Because the cross-sectional shape functions are expressed in closed form in HoBT, there is no need to derive them even if the sectional properties of thin-walled box beam change. Furthermore, so far only the HoBT offers the explicit joint relations for thin-walled beams having angled joints, which will be critically useful for the buckling analysis of such beams in the future.

In order to perform the buckling analysis of box beams by using the HoBT, the selected deformation shapes of the employed DOFs (see Table 1) are grouped into sets of deformations, each of which consists of extension, major-axis bending, minor-axis bending, and torsion. In the present study, we use up to three sets of DOFs (or sectional mode shapes). In order to describe the internal stress and displacement in each wall of a box beam, the plane stress assumption and the Kirchhoff-Love plate theory are used. Therefore, if the number of DOFs increases, the results obtained by the HoBT-based buckling analysis approach the results obtained by the plate theory-based buckling analysis. Note that we do not use any assumption to perform the pre-buckling stress analysis. Therefore, the present results for buckling problems are expected to be sufficiently close to those obtained by the shell-based analysis.

With respect to the remaining sections, Sec. 2 presents the procedure to define the displacement field in the framework of the HoBT and also the procedure to calculate the pre-buckling stress. In Sec. 3, the detailed buckling analysis formulation is given in which three sets of DOFs in the HoBT are considered. In order to perform numerical investigations, the finite element equation is derived in Sec. 4. The displacement fields are interpolated by the Hermitian cubic functions. If piecewise linear functions are used as opposed to the Hermitian cubic functions, a few of the strain components necessary for buckling analysis cannot be computed, resulting in deteriorated solution accuracy. Sec. 5 presents numerical results for the buckling analysis of box beams subject to various loadings, namely axial, torsional, and bending loadings. For each case, the length-to-height ratios of the beams were varied from 1 to 100. The effects of boundary conditions were also investigated. Furthermore, we considered arbitrary loading cases to demonstrate the generality of the developed method. The effects of the sectional aspect ratio and the thickness were also examined. The accuracy of the numerical results obtained by the HoBT-based proposed formulation is compared with those obtained by using shell finite elements (ABAQUS).

2. Employed higher-order beam theory (HoBT)

2.1 Displacement field by HoBT

The higher-order beam theory (HoBT) uses one-dimensional (1D) beam DOFs and the corresponding sectional shape functions to express three-dimensional displacements at an arbitrary point on the beam cross-section [33]. As shown in Fig. 1, the geometry of a cross-section in a beam is described in terms of the global coordinates (x, y, z) while the location of an arbitrary point on a cross-section is expressed in terms of the local coordinates (n, s, z) assigned for each edge. The origin of the local coordinate system is located at the center of each edge, and n and s denote the outward normal coordinate and the tangential coordinate along the centerline of the contour, respectively. The sectional shape functions that describe the cross-sectional deformations are separately expressed for each edge by using the local coordinates. Table 1 shows a total of 50 higher-order beam DOFs employed for the buckling analysis of box beams under general loadings. They are derived by extending the method in Ref. [38]. There are 6 DOFs of the classical beam theory and additional 44 DOFs associated with the cross-sectional deformations [33-35, 38]. The employed DOFs in Table 1 represent all possible types of deformations in a box beam (extensional, bending, and torsional). The x- and y-directional bending deformations are those associated with the overall transverse displacement of the cross-section along the x- and y-axes, respectively. In Table 1, U, θ, χ, W and η represent the classical beam translations, classical beam rotations, cross-sectional distortions,

warping, and plate bending deformations, respectively. The subscripts *e*, *bx*, *by* and *t* are used in Table 1 to indicate that the subscribed kinematic measures (i.e., U, θ, χ and W) are related to the extension, *x*-directional bending, *y*-directional bending, and torsion, respectively.

In the HoBT, the three-dimensional (3D) displacements at a point on the centerline of the cross-section are expressed by summing the products of the 1D deformation measure and its corresponding shape function as follows:

$$\begin{aligned} u_n(s,z) &= \psi_n^{U_x}(s)U_x(z) + \psi_n^{\chi_{bx1}}(s)\chi_{bx1}(z) + \cdots + \psi_n^{\eta_{t3\_2}}(s)\eta_{t3\_2}(z) \\ u_s(s,z) &= \psi_s^{U_x}(s)U_x(z) + \psi_s^{\chi_{bx1}}(s)\chi_{bx1}(z) + \cdots + \psi_s^{\chi_{t3}}(s)\chi_{t3}(z) \\ u_z(s,z) &= \psi_z^{\theta_y}(s)\theta_y(z) + \psi_z^{W_{bx1}}(s)W_{bx1}(z) + \cdots + \psi_z^{W_{t3}}(s)W_{t3}(z) \end{aligned} \tag{1a}$$

or

$$u_n = \boldsymbol{\psi}_n\mathbf{d}, \qquad u_s = \boldsymbol{\psi}_s\mathbf{d}, \qquad u_z = \boldsymbol{\psi}_z\mathbf{d} \tag{1b}$$

where $u_i(i=n,s,z)$ refers to the *i*-directional displacement and ψ_i^{α} $(i=n,s,z;\ \alpha = U_z,\cdots,\chi_{e1},\cdots,W_{e1},\cdots,\eta_{e1\_1},\cdots)$ denotes the sectional shape function that describes the *i*-directional deformation caused by unit magnitude of α. Table 1 illustrates all the sectional shape functions. Eq. (1b) is a compact form of Eq. (1a) that is expressed in terms of the shape function row vector, $\boldsymbol{\psi}_i(i=n,s,z)$ and the 1D deformation measure column vector, $\mathbf{d} = \{U_z\cdots\chi_{e1}\cdots W_{e1}\cdots \eta_{e1\_1}\cdots\}^T$. To obtain all of the shape functions in Table 1, we used the method developed in Ref. [38].

By using Eq. (1), 3D displacements $(\tilde{u}_n, \tilde{u}_s, \tilde{u}_z)$ for a generic point on a cross-section can be obtained as:

$$\tilde{u}_n(n,s,z) \approx u_n,\ \ \tilde{u}_s(n,s,z) \approx u_s - n\frac{\partial u_n}{\partial s},\ \ \tilde{u}_z(n,s,z) \approx u_z - n\frac{\partial u_n}{\partial z} \tag{2a}$$

or

$$\tilde{u}_n = \boldsymbol{\psi}_n\mathbf{d},\ \ \tilde{u}_s = \boldsymbol{\psi}_s\mathbf{d} - n\frac{\partial\boldsymbol{\psi}_n}{\partial s}\mathbf{d},\ \ \tilde{u}_z = \boldsymbol{\psi}_z\mathbf{d} - n\boldsymbol{\psi}_n\frac{\partial\mathbf{d}}{\partial z}. \tag{2b}$$

Eq. (2) is based on the Kirchhoff–Love plate theory in which the rotations of thin-walls caused by the *n*-directional deflection are considered. It should be noted that the last term in the expression for $\tilde{u}_z$ represents the rotation about the *s*-axis due to distortion. In order to consider the contribution of the $\partial(\bullet)/\partial z$ term in Eq. (2b), C^1 continuity functions, such as the Hermite cubic interpolation function, must be employed for finite element implementation.

With respect to accurate buckling analysis, both buckled deformations and pre-buckling stress should be accurately calculated. One advantage of using the higher-order beam theory adopting the kinematic variables (and the associated sectional shapes) in Table 1 is that the sectional deformations representing plate bending motions are also included. Because plate bending deformation arises due to compression or shearing loads acting on the edge when buckling occurs in thin-walled beams, the corresponding sectional deformations must be included. Note that the employed cross-sectional shape functions in Table 1 are orthogonal to each other and hierarchically constructed. Therefore, the solution accuracy level can be adjusted by selecting a different number of the cross-sectional degrees of freedom in the order shown in Table 1.

2.2 Stress analysis with HoBT

In this section, the stress analysis procedure is presented because pre-buckling stress analysis must be performed for buckling analysis. First, we express strain fields in the framework of the higher-order beam theory. Because walls forming a box beam are extremely thin, the plane stress assumption can be used for strain–stress analysis as follows:

$$\begin{aligned} \varepsilon_{ss}(n,s,z) &= \frac{\partial\tilde{u}_s}{\partial s} \approx \frac{\partial\boldsymbol{\psi}_s}{\partial s}\mathbf{d} - n\frac{\partial^2\boldsymbol{\psi}_n}{\partial s^2}\mathbf{d} \\ \varepsilon_{zz}(n,s,z) &= \frac{\partial\tilde{u}_z}{\partial z} \approx \boldsymbol{\psi}_z\frac{\partial\mathbf{d}}{\partial z} - n\boldsymbol{\psi}_n\frac{\partial^2\mathbf{d}}{\partial z^2} \\ 2\varepsilon_{sz}(n,s,z) &= \frac{\partial\tilde{u}_s}{\partial z} + \frac{\partial\tilde{u}_z}{\partial s} \approx \boldsymbol{\psi}_s\frac{\partial\mathbf{d}}{\partial z} + \frac{\partial\boldsymbol{\psi}_z}{\partial s}\mathbf{d} - 2n\frac{\partial\boldsymbol{\psi}_n}{\partial s}\frac{\partial\mathbf{d}}{\partial z} \end{aligned} \tag{3}$$

and

$$\begin{Bmatrix}\sigma_{ss}\\ \sigma_{zz}\\ \sigma_{sz}\end{Bmatrix} = \frac{E}{1-\nu^2}\begin{bmatrix}1 & \nu & 0\\ \nu & 1 & 0\\ 0 & 0 & \dfrac{1-\nu}{2}\end{bmatrix}\begin{Bmatrix}\varepsilon_{ss}\\ \varepsilon_{zz}\\ 2\varepsilon_{sz}\end{Bmatrix} \quad \text{or} \quad \boldsymbol{\sigma} = \mathbf{C}\boldsymbol{\varepsilon} \tag{4}$$

where E and ν denote Young's modulus and Poisson's ratio, respectively. The symbols $\boldsymbol{\sigma}$, $\boldsymbol{\varepsilon}$ and $\mathbf{C}$ denote the stress vector, strain vector, and elasticity matrix, respectively. By using Eqs. (3) and (4), the internal strain energy (Π_{SE}) is defined as:

$$\begin{aligned} \Pi_{SE} &= \int_V \frac{1}{2}\boldsymbol{\sigma}^T\boldsymbol{\varepsilon}\,dV \\ &= \int_V \frac{1}{2}\boldsymbol{\varepsilon}^T\mathbf{C}\boldsymbol{\varepsilon}\,dV \\ &= \int_V \frac{1}{2}\Big(\mathbf{d}^T\mathbf{D}_1\mathbf{d} + \mathbf{d}^T\mathbf{D}_2\mathbf{d}_{,z} + \mathbf{d}^T\mathbf{D}_3\mathbf{d}_{,zz} \\ &\qquad + \mathbf{d}_{,z}^T\mathbf{D}_4\mathbf{d}_{,z} + \mathbf{d}_{,z}^T\mathbf{D}_5\mathbf{d}_{,zz} + \mathbf{d}_{,zz}^T\mathbf{D}_6\mathbf{d}_{,zz}\Big)\,dV \\ &= \int_z \frac{1}{2}\Big(\mathbf{d}^T\big[\mathbf{D}_1\big]\mathbf{d} + \mathbf{d}^T\big[\mathbf{D}_2\big]\mathbf{d}_{,z} + \mathbf{d}^T\big[\mathbf{D}_3\big]\mathbf{d}_{,zz} \\ &\qquad + \mathbf{d}_{,z}^T\big[\mathbf{D}_4\big]\mathbf{d}_{,z} + \mathbf{d}_{,z}^T\big[\mathbf{D}_5\big]\mathbf{d}_{,zz} + \mathbf{d}_{,zz}^T\big[\mathbf{D}_6\big]\mathbf{d}_{,zz}\Big)dz \end{aligned} \tag{5}$$

where

Table 1. The degrees of freedom and the corresponding cross-sectional (deformation) mode shapes used in the present HoBT-based buckling analysis.

	Beam DOFs	The first set of cross-sectional DOFs	The second set of cross-sectional DOFs	The third set of cross-sectional DOFs
Extensional DOFs	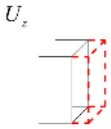	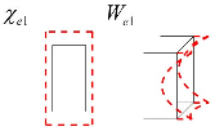	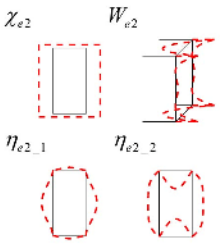	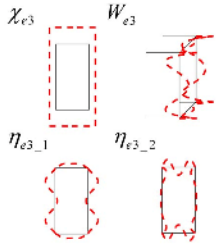
Bending DOFs (x-directional)	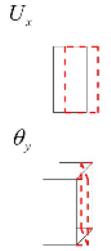	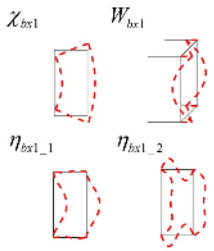	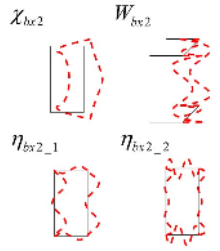	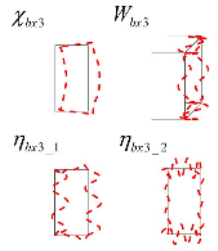
Bending DOFs (y-directional)	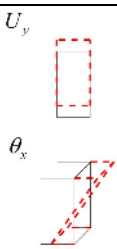	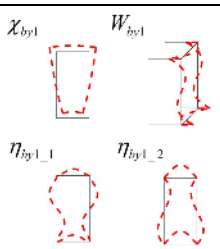	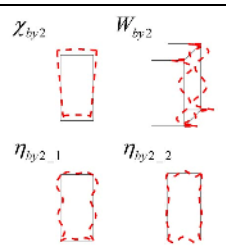	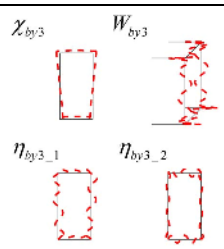
Torsional DOFs	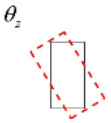	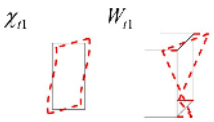	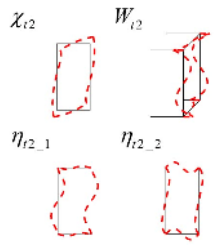	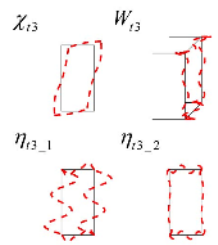

$$\mathbf{D}_1 = E_1\left\{\left(\boldsymbol{\psi}_{s,s} - n\boldsymbol{\psi}_{n,ss}\right)^T\left(\boldsymbol{\psi}_{s,s} - n\boldsymbol{\psi}_{n,ss}\right) + \frac{1-\nu}{2}\boldsymbol{\psi}_{z,s}^T\boldsymbol{\psi}_{z,s}\right\}$$

$$\mathbf{D}_2 = E_1\left\{2\nu\left(\boldsymbol{\psi}_{s,s} - n\boldsymbol{\psi}_{n,ss}\right)^T\boldsymbol{\psi}_z + (1-\nu)\boldsymbol{\psi}_{z,s}^T\left(\boldsymbol{\psi}_s - 2n\boldsymbol{\psi}_{n,s}\right)\right\}$$

$$\mathbf{D}_3 = E_1\left\{2\nu\left(\boldsymbol{\psi}_{s,s} - n\boldsymbol{\psi}_{n,ss}\right)^T\left(-n\boldsymbol{\psi}_n\right)\right\}$$

$$\mathbf{D}_4 = E_1\left\{\boldsymbol{\psi}_z^T\boldsymbol{\psi}_z + \frac{1-\nu}{2}\left(\boldsymbol{\psi}_s - 2n\boldsymbol{\psi}_{n,s}\right)^T\left(\boldsymbol{\psi}_s - 2n\boldsymbol{\psi}_{n,s}\right)\right\}$$

$$\mathbf{D}_5 = E_1\left\{\boldsymbol{\psi}_z^T\left(-n\boldsymbol{\psi}_n\right)\right\}$$

$$\mathbf{D}_6 = E_1\left(n^2\boldsymbol{\psi}_n^T\boldsymbol{\psi}_n\right).$$

In Eq. (5), the expression $[\bullet]$ implies the integration over cross-sectional area (i.e., $[\bullet]=\int_A \bullet\, dA$). Given that $\mathbf{D}_i\ (i=1,\cdots,6)$ are the known functions expressed in terms of the cross-sectional shape functions, they can be directly integrated with respect to local cross-sectional coordinates (n,s). Furthermore, the external work performed by applied forces $(\mathbf{f}_{surf}, \mathbf{f}_{body})$ is expressed as:

$$\begin{aligned}\Pi_{external} &= -\sum_k\left(\int_A \mathbf{f}_{surf}{}^T\mathbf{u}\, dA\right)\Big|_{z=z_k} - \int_V \mathbf{f}_{body}{}^T\mathbf{u}\, dV \\ &= -\sum_k\left(\left[\mathbf{f}_{surf}{}^T\boldsymbol{\psi}\right]\cdot\mathbf{d}\right)\Big|_{z=z_k} - \int_z\left[\mathbf{f}_{body}{}^T\boldsymbol{\psi}\right]\cdot\mathbf{d}\, dz\end{aligned} \tag{6}$$

where $\mathbf{f}_{surf}(n,s,z) = \left\{\left(f_{surf}\right)_n \quad \left(f_{surf}\right)_s \quad \left(f_{surf}\right)_z\right\}^T$ and $\mathbf{f}_{body}(n,s,z) = \left\{\left(f_{body}\right)_n \quad \left(f_{body}\right)_s \quad \left(f_{body}\right)_z\right\}^T$ denote the surface and body forces, respectively. The symbol $\boldsymbol{\psi} = \left[\boldsymbol{\psi}_n \quad \boldsymbol{\psi}_s \quad \boldsymbol{\psi}_z\right]^T$ denotes the shape function matrix. In Eq. (6), the quantities inside the square brackets denoting the integration operation ($\left[\mathbf{f}_{surf}{}^T\boldsymbol{\psi}\right]$ or $\left[\mathbf{f}_{body}{}^T\boldsymbol{\psi}\right]$) correspond to the generalized beam

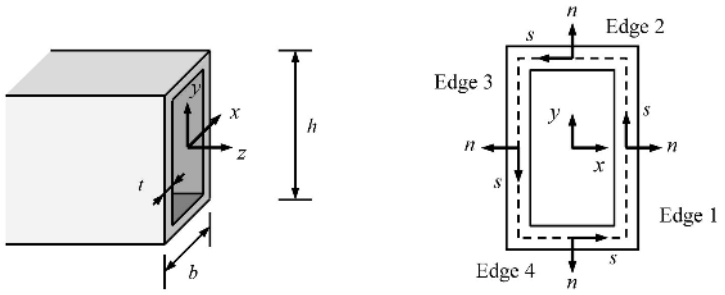

(a) (b)

Fig. 1. (a) Global; (b) local coordinates of a thin-walled box beam. The origins of the local coordinate system are placed at the center of each edge.

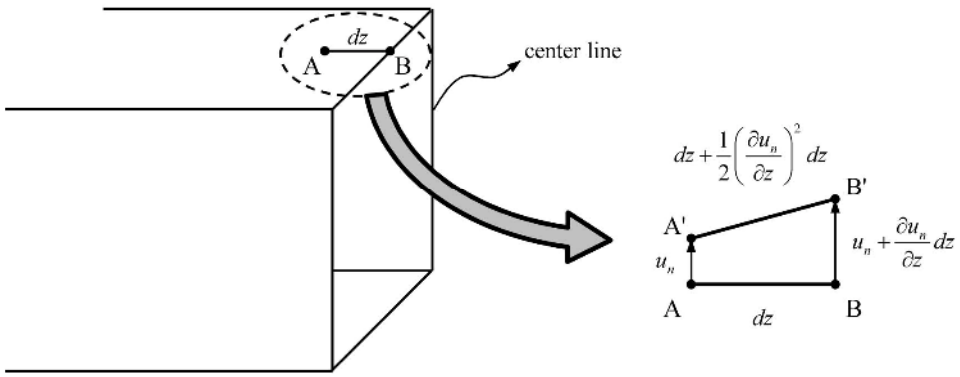

Fig. 2. Infinitesimal length of a fiber on the middle surface of the beam section: $\overline{\mathrm{AB}}$: Undeformed infinitesimal fiber; $\overline{\mathrm{A'B'}}$: Deformed infinitesimal fiber after bending deflection occurs due to u_n .

force vectors. They are the energy-conjugates of the 1D deformation measure vector, **d**. In order to express the governing equation for static analysis, the following minimum total potential energy principle is used:

$$\begin{aligned}\delta\Pi_{total} &= \delta\Pi_{SE} + \delta\Pi_{external} \\ &= \int_z \frac{1}{2}\Big(2\delta\mathbf{d}^T\left[\mathbf{D}_1\right]\mathbf{d} + \delta\mathbf{d}^T\left[\mathbf{D}_2\right]\mathbf{d}_{,z} + \delta\mathbf{d}_{,z}^T\left[\mathbf{D}_2\right]^T\mathbf{d} \\ &\quad + \delta\mathbf{d}^T\left[\mathbf{D}_3\right]\mathbf{d}_{,zz} + \delta\mathbf{d}_{,zz}^T\left[\mathbf{D}_3\right]^T\mathbf{d} + 2\delta\mathbf{d}_{,z}^T\left[\mathbf{D}_4\right]\mathbf{d}_{,z} \\ &\quad + \delta\mathbf{d}_{,z}^T\left[\mathbf{D}_5\right]\mathbf{d}_{,zz} + \delta\mathbf{d}_{,zz}^T\left[\mathbf{D}_5\right]^T\mathbf{d}_{,z} + 2\delta\mathbf{d}_{,zz}^T\left[\mathbf{D}_6\right]\mathbf{d}_{,zz}\Big)\,dz \\ &\quad + \left\{-\sum_k\Big(\left[\mathbf{f}_{surf}{}^T\boldsymbol{\psi}\right]\cdot\delta\mathbf{d}\Big)\Big|_{z=z_k} - \int_z\left[\mathbf{f}_{body}{}^T\boldsymbol{\psi}\right]\cdot\delta\mathbf{d}\,dz\right\} \\ &= 0\,.\end{aligned} \tag{7}$$

The displacement field that satisfies Eq. (7) is the solution for a box beam subjected to $\mathbf{f}_{surf}$ and $\mathbf{f}_{body}$. Once the displacement field is obtained from Eq. (7), the stress field can be calculated by using Eqs. (3) and (4).

3. Buckling analysis based on HoBT

Buckling patterns can differ based on boundary/loading conditions and beam dimensions. In case of local buckling, the beam deformations are mainly characterized by distortion and warping without rigid-body motions of the beam cross-section. (Therefore, one may assume $U_x = U_y = U_z = \theta_x = \theta_y = \theta_z \approx 0$ for local buckling.) Even in global buckling, warping and distortional deformations are generally significant. Therefore, the buckling behavior of a thin-walled box beam must be analyzed by considering the plate behavior of the four walls constituting a box beam. In this study, the linearized buckling analysis will be considered by taking into account the geometrical nonlinearity.

When buckling occurs, each wall of a box beam experiences dominant bending that potentially induces normal and shear strains everywhere [40]. The corresponding geometric nonlinear strains $\bar{\varepsilon}_{ss}(n,s,z)$, $\bar{\varepsilon}_{zz}(n,s,z)$ and $\bar{\varepsilon}_{sz}(n,s,z)$, as expressed in terms of the von Kármán strain, are expressed for buckling analysis:

$$\begin{aligned}\bar{\varepsilon}_{ss}(n,s,z) &= \frac{1}{2}\left(\frac{\partial\tilde{u}_n}{\partial s}\right)^2 + \frac{1}{2}\left(\frac{\partial\tilde{u}_z}{\partial s}\right)^2 \\ &\approx \frac{1}{2}\left(\frac{\partial u_n}{\partial s}\right)^2 + \frac{1}{2}\left(\frac{\partial u_z}{\partial s} - n\frac{\partial^2 u_n}{\partial s\partial z}\right)^2 \\ \bar{\varepsilon}_{zz}(n,s,z) &= \frac{1}{2}\left(\frac{\partial\tilde{u}_n}{\partial z}\right)^2 + \frac{1}{2}\left(\frac{\partial\tilde{u}_s}{\partial z}\right)^2 \\ &\approx \frac{1}{2}\left(\frac{\partial u_n}{\partial z}\right)^2 + \frac{1}{2}\left(\frac{\partial u_s}{\partial z} - n\frac{\partial^2 u_n}{\partial s\partial z}\right)^2 \\ 2\bar{\varepsilon}_{sz}(n,s,z) &= \frac{\partial\tilde{u}_n}{\partial s}\frac{\partial\tilde{u}_n}{\partial z} \approx \frac{\partial u_n}{\partial s}\frac{\partial u_n}{\partial z}\,.\end{aligned} \tag{8}$$

Fig. 2 sketches the mechanism how the nonlinear strain is

developed.

The geometric nonlinear strain fields in Eq. (8) are combined with the pre-buckling stress fields to calculate the work performed by buckling. By using Eq. (8), the work (Π_W) performed by the nonlinear strain is defined as follows:

$$\begin{aligned}\Pi_{buckling} &= -\int_V \lambda_{cr}\boldsymbol{\sigma}_{pre}^T\bar{\boldsymbol{\varepsilon}}\,dV \\ &= -\lambda_{cr}\int_V\left\{\left(\sigma_{pre}\right)_{ss}\bar{\varepsilon}_{ss}+\left(\sigma_{pre}\right)_{zz}\bar{\varepsilon}_{zz}+\left(\sigma_{pre}\right)_{sz}\left(2\bar{\varepsilon}_{sz}\right)\right\}dV \\ &= -\lambda_{cr}\int_V\left(\mathbf{d}^T\mathbf{P}_1\mathbf{d}+\mathbf{d}^T\mathbf{P}_2\mathbf{d}_{,z}+\mathbf{d}_{,z}^T\mathbf{P}_3\mathbf{d}_{,z}\right)dV \\ &= -\lambda_{cr}\int_z\left(\mathbf{d}^T\left[\mathbf{P}_1\right]\mathbf{d}+\mathbf{d}^T\left[\mathbf{P}_2\right]\mathbf{d}_{,z}+\mathbf{d}_{,z}^T\left[\mathbf{P}_3\right]\mathbf{d}_{,z}\right)dz\end{aligned} \tag{9}$$

where

$$\begin{aligned}\mathbf{P}_1 &= \frac{1}{2}\left(\sigma_{pre}\right)_{ss}\left(\boldsymbol{\psi}_{n,s}^T\boldsymbol{\psi}_{n,s}+\boldsymbol{\psi}_{z,s}^T\boldsymbol{\psi}_{z,s}\right) \\ \mathbf{P}_2 &= \left(\sigma_{pre}\right)_{ss}\boldsymbol{\psi}_{z,s}^T\left(-n\boldsymbol{\psi}_{n,s}\right)+\left(\sigma_{pre}\right)_{sz}\boldsymbol{\psi}_{n,s}^T\boldsymbol{\psi}_n \\ \mathbf{P}_3 &= \frac{1}{2}\left(\sigma_{pre}\right)_{ss}\left(-n\boldsymbol{\psi}_{n,s}\right)^T\left(-n\boldsymbol{\psi}_{n,s}\right) \\ &\quad+\frac{1}{2}\left(\sigma_{pre}\right)_{zz}\left\{\boldsymbol{\psi}_n^T\boldsymbol{\psi}_n+\left(\boldsymbol{\psi}_s-n\boldsymbol{\psi}_{n,s}\right)^T\left(\boldsymbol{\psi}_s-n\boldsymbol{\psi}_{n,s}\right)\right\}.\end{aligned}$$

In Eq. (9), λ_{cr}, $\boldsymbol{\sigma}_{pre}$ and $\bar{\boldsymbol{\varepsilon}}$ denote the buckling load scale factor, pre-buckling stress vector, and geometric nonlinear strain vector, respectively. The pre-buckling stress vector σ_{pre} is calculated as:

$$\boldsymbol{\sigma}_{pre} = \mathbf{C}\cdot\boldsymbol{\varepsilon}\left(\mathbf{d}_{pre}\right) \tag{10}$$

where $\mathbf{d}_{pre}$ denotes the vector of deformation measures calculated by a linear static analysis for a given loading and boundary condition by using Eq. (7). The pre-buckling stress vector describes the stress distribution in a box beam immediately before buckling occurs.

The governing equation for buckling analysis is obtained by using the total potential energy Π_{total} that is the sum of the terms in Eqs. (5) and (9). We consider the variation in Π_{total} as follows:

$$\begin{aligned}\delta\Pi_{total} &= \delta\Pi_{SE}+\delta\Pi_{buckling} \\ &= \int_V\delta\boldsymbol{\varepsilon}^T\mathbf{C}\boldsymbol{\varepsilon}\,dV-\lambda\int_V\boldsymbol{\sigma}_{pre}^T\delta\bar{\boldsymbol{\varepsilon}}\,dV \\ &= \int_z\frac{1}{2}\left(2\delta\mathbf{d}^T\left[\mathbf{D}_1\right]\mathbf{d}+\delta\mathbf{d}^T\left[\mathbf{D}_2\right]\mathbf{d}_{,z}+\delta\mathbf{d}_{,z}^T\left[\mathbf{D}_2\right]^T\mathbf{d}\right. \\ &\quad+\delta\mathbf{d}^T\left[\mathbf{D}_3\right]\mathbf{d}_{,zz}+\delta\mathbf{d}_{,zz}^T\left[\mathbf{D}_3\right]^T\mathbf{d}+2\delta\mathbf{d}_{,z}^T\left[\mathbf{D}_4\right]\mathbf{d}_{,z} \\ &\quad\left.+\delta\mathbf{d}_{,z}^T\left[\mathbf{D}_5\right]\mathbf{d}_{,zz}+\delta\mathbf{d}_{,zz}^T\left[\mathbf{D}_5\right]^T\mathbf{d}_{,z}+2\delta\mathbf{d}_{,zz}^T\left[\mathbf{D}_6\right]\mathbf{d}_{,zz}\right)dz \\ &\quad-\lambda\int_z\left(2\delta\mathbf{d}^T\left[\mathbf{P}_1\right]\mathbf{d}+\delta\mathbf{d}^T\left[\mathbf{P}_2\right]\mathbf{d}_{,z}\right. \\ &\quad\left.+\delta\mathbf{d}_{,z}^T\left[\mathbf{P}_2\right]^T\mathbf{d}+2\delta\mathbf{d}_{,z}^T\left[\mathbf{P}_3\right]\mathbf{d}_{,z}\right)dz.\end{aligned} \tag{11}$$

If the value of Eq. (11) is less than zero, a thin-walled beam is in an unstable state. Therefore, the unstable state corresponds to the onset of buckling. Based on this argument, the condition for the occurrence of buckling [40] is expressed as:

$$\begin{aligned}\delta\Pi_{total} &= \delta\Pi_{SE}+\delta\Pi_{buckling} \\ &= \int_V\delta\boldsymbol{\varepsilon}^T\mathbf{C}\boldsymbol{\varepsilon}\,dV-\lambda_{cr}\int_V\boldsymbol{\sigma}_{pre}^T\delta\bar{\boldsymbol{\varepsilon}}\,dV=0.\end{aligned} \tag{12}$$

The variation in the total potential energy always passes through a neutrally stable state ($\delta\Pi_{total}=0$) when buckling occurs. Therefore, by multiplying the prescribed unit load and critical scale factor λ_{cr} calculated from Eq. (12), a critical load can be obtained as:

$$P_{cr} = \lambda_{cr}P_{pre} \tag{13}$$

where P_{pre} denotes a prescribed unit load corresponding to the given loading and boundary conditions. The prescribed load $\left(\left[\mathbf{f}_{surf}{}^T\boldsymbol{\psi}\right],\left[\mathbf{f}_{body}{}^T\boldsymbol{\psi}\right]\right)$ is defined consistently with the HoBT.

4. Finite element formulation

This section presents a finite element formulation for numerical analysis based on the governing equation derived in the previous section. In the investigation, a Hermite cubic interpolation function that satisfies C^1 continuity is used to interpolate the deformation inside the discretized analysis domain. If a linear interpolation is used as opposed to the Hermite cubic interpolation function, the sectional rotation from the bending term of ε_{zz} in Eq. (3) disappears. Subsequently, omitting the energy corresponding to the term leads to inaccurate results. Thus, the 1D deformation measure α ($=U_z,\chi_{ie1},\cdots,\chi_{ot2}$) in Eq. (1) is interpolated by using the Hermite cubic interpolation function as:

$$\alpha(z) = H_1(z)\cdot\alpha_1+H_2(z)\cdot\alpha_1'+H_3(z)\cdot\alpha_2+H_4(z)\cdot\alpha_2' \tag{14}$$

where

$$\begin{aligned}H_1 &= \frac{1}{(z_2-z_1)^3}\left\{2z^3-3(z_2-z_1)z^2+(z_2-z_1)^3\right\} \\ H_2 &= \frac{1}{(z_2-z_1)^3}\left\{z^3-2(z_2-z_1)z^2+(z_2-z_1)^2z\right\} \\ H_3 &= \frac{1}{(z_2-z_1)^3}\left\{-2z^3+3(z_2-z_1)z^2\right\} \\ H_4 &= \frac{1}{(z_2-z_1)^3}\left\{z^3-(z_2-z_1)z^2\right\}\end{aligned}$$

$$(z_1\le z\le z_2).$$

In Eq. (14), $\alpha_i\,(i=1,2)$ denotes a nodal deformation measure at node i, α_i' denotes a partial derivative of α_i

about z $\left(\alpha_i' = \partial\alpha_i / \partial z\right)$, and z_i denotes the z coordinate of node i. When the Hermite cubic interpolation function is used, α_i' is treated as an independent kinematic DOF. Therefore, Eq. (14) is expressed in compact form as:

$$\mathbf{d} = \mathbf{HU} \tag{15}$$

where

$$\mathbf{U} = \left[\{U_z\}_1 \quad \{U_z'\}_1 \quad \{\chi_{e1}\}_1 \quad \cdots \quad \{U_z\}_2 \quad \cdots \quad \{\eta_{t3}'\}_2\right]^T.$$

In Eq. (15), $\mathbf{H}$ denotes an interpolation matrix and $\mathbf{U}$ is a nodal displacement vector. The substitution of $\mathbf{d}$ in Eq. (15) into Eq. (3) yields the expressions of $\boldsymbol{\varepsilon}$ in terms of $\mathbf{U}$:

$$\boldsymbol{\varepsilon} = \begin{Bmatrix} \varepsilon_{ss} \\ \varepsilon_{zz} \\ 2\varepsilon_{sz} \end{Bmatrix} = \begin{Bmatrix} \dfrac{\partial \boldsymbol{\psi}_s}{\partial s}\mathbf{HU} - n\dfrac{\partial^2 \boldsymbol{\psi}_n}{\partial s^2}\mathbf{HU} \\ \boldsymbol{\psi}_z \dfrac{\partial \mathbf{H}}{\partial z}\mathbf{U} - n\boldsymbol{\psi}_n \dfrac{\partial^2 \mathbf{H}}{\partial z^2}\mathbf{U} \\ \boldsymbol{\psi}_s \dfrac{\partial \mathbf{H}}{\partial z}\mathbf{U} + \dfrac{\partial \boldsymbol{\psi}_z}{\partial s}\mathbf{HU} - 2n\dfrac{\partial \boldsymbol{\psi}_n}{\partial s}\dfrac{\partial \mathbf{H}}{\partial s}\mathbf{U} \end{Bmatrix} = \mathbf{BU} \tag{16}$$

where $\mathbf{B}$ denotes a strain–displacement matrix. By substituting Eq. (16) into Eq. (5), the variation in the strain energy term ($\delta\Pi_{SE}$) can be expressed in a discretized form as:

$$\begin{aligned} \delta\Pi_{SE} &= \int_V \delta\boldsymbol{\varepsilon}^{\mathrm{T}}\mathbf{C}\boldsymbol{\varepsilon}\, dV = \int_V \delta\mathbf{U}^{\mathrm{T}}\mathbf{B}^{\mathrm{T}}\mathbf{CBU}\, dV \\ &= \delta\mathbf{U}^{\mathrm{T}}\left(\int_V \mathbf{B}^{\mathrm{T}}\mathbf{CB}\, dV\right)\mathbf{U} \\ &= \delta\mathbf{U}^{\mathrm{T}}\mathbf{KU} \end{aligned} \tag{17}$$

where $\mathbf{K}$ denotes a stiffness matrix. Similarly, the discretized geometric nonlinear strain is obtained in discretized form by inserting Eq. (15) into Eq. (8):

$$\bar{\boldsymbol{\varepsilon}} = \begin{Bmatrix} \bar{\varepsilon}_{ss} \\ \bar{\varepsilon}_{zz} \\ 2\bar{\varepsilon}_{sz} \end{Bmatrix} = \begin{Bmatrix} \dfrac{1}{2}\left(\dfrac{\partial \boldsymbol{\psi}_n}{\partial s}\mathbf{HU}\right)^2 + \dfrac{1}{2}\left(\dfrac{\partial \boldsymbol{\psi}_z}{\partial s}\mathbf{HU} - n\dfrac{\partial \boldsymbol{\psi}_n}{\partial s}\dfrac{\partial \mathbf{H}}{\partial z}\mathbf{U}\right)^2 \\ \dfrac{1}{2}\left(\boldsymbol{\psi}_n \dfrac{\partial \mathbf{H}}{\partial z}\mathbf{U}\right)^2 + \dfrac{1}{2}\left(\boldsymbol{\psi}_s \dfrac{\partial \mathbf{H}}{\partial z}\mathbf{U} - n\dfrac{\partial \boldsymbol{\psi}_n}{\partial s}\dfrac{\partial \mathbf{H}}{\partial z}\mathbf{U}\right)^2 \\ \left(\dfrac{\partial \boldsymbol{\psi}_n}{\partial s}\mathbf{HU}\right)\left(\boldsymbol{\psi}_n \dfrac{\partial \mathbf{H}}{\partial z}\mathbf{U}\right) \end{Bmatrix}$$

$$= \frac{1}{2}\begin{Bmatrix} \mathbf{U}^T\left[\mathbf{H}^T \dfrac{\partial \boldsymbol{\psi}_n}{\partial s}^T \dfrac{\partial \boldsymbol{\psi}_n}{\partial s}\mathbf{H} + \left(\mathbf{H}^T \dfrac{\partial \boldsymbol{\psi}_z}{\partial s}^T - n\dfrac{\partial \mathbf{H}}{\partial z}^T \dfrac{\partial \boldsymbol{\psi}_n}{\partial s}^T\right)\left(\dfrac{\partial \boldsymbol{\psi}_z}{\partial s}\mathbf{H} - n\dfrac{\partial \boldsymbol{\psi}_n}{\partial s}\dfrac{\partial \mathbf{H}}{\partial z}\right)\right]\mathbf{U} \\ \mathbf{U}^T\left[\dfrac{\partial \mathbf{H}}{\partial z}^T \boldsymbol{\psi}_n{}^T\boldsymbol{\psi}_n \dfrac{\partial \mathbf{H}}{\partial z} + \left(\dfrac{\partial \mathbf{H}}{\partial z}^T \boldsymbol{\psi}_s{}^T - n\dfrac{\partial \mathbf{H}}{\partial z}^T \dfrac{\partial \boldsymbol{\psi}_n}{\partial s}^T\right)\left(\boldsymbol{\psi}_s \dfrac{\partial \mathbf{H}}{\partial z} - n\dfrac{\partial \boldsymbol{\psi}_n}{\partial s}\dfrac{\partial \mathbf{H}}{\partial z}\right)\right]\mathbf{U} \\ \mathbf{U}^T\left(\mathbf{H}^T \dfrac{\partial \boldsymbol{\psi}_n}{\partial s}^T \boldsymbol{\psi}_n \dfrac{\partial \mathbf{H}}{\partial z} + \dfrac{\partial \mathbf{H}}{\partial z}^T \boldsymbol{\psi}_n{}^T \dfrac{\partial \boldsymbol{\psi}_n}{\partial s}\mathbf{H}\right)\mathbf{U} \end{Bmatrix}$$

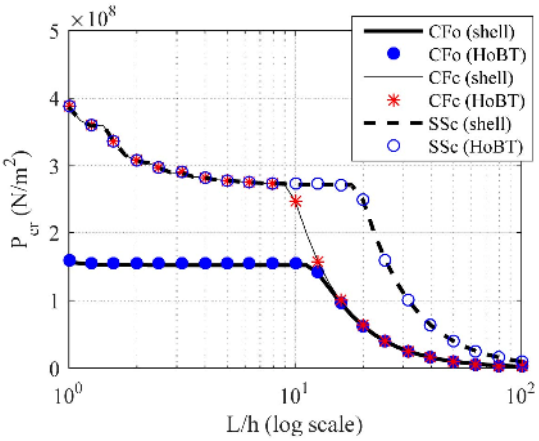

Fig. 3. The effects of the boundary conditions on P_{cr} (critical load) for case study 1.

$$= \frac{1}{2}\begin{Bmatrix} \mathbf{U}^T\mathbf{B}_{ss}\mathbf{U} \\ \mathbf{U}^T\mathbf{B}_{zz}\mathbf{U} \\ \mathbf{U}^T\mathbf{B}_{sz}\mathbf{U} \end{Bmatrix} \tag{18}$$

where $\mathbf{B}_{ij}\,(i, j = s, z)$ is defined as the strain–displacement matrix for $\bar{\varepsilon}_{ij}$. Substituting Eq. (18) into the variation of Eq. (9) yields the following expression:

$$\begin{aligned} \delta\Pi_{buckling} &= -\lambda\int_V \boldsymbol{\sigma}_{pre}{}^{\mathrm{T}}\delta\boldsymbol{\varepsilon}'\, dV \\ &= -\lambda\int_V \delta\mathbf{U}^{\mathrm{T}}\left\{\left(\sigma_{pre}\right)_{ss}\mathbf{B}_{ss} + \left(\sigma_{pre}\right)_{zz}\mathbf{B}_{zz} + \left(\sigma_{pre}\right)_{sz}\mathbf{B}_{sz}\right\}\mathbf{U}\, dV \\ &= -\lambda\,\delta\mathbf{U}^{\mathrm{T}}\left\{\int_V \left(\sigma_{pre}\right)_{ss}\mathbf{B}_{ss} + \left(\sigma_{pre}\right)_{zz}\mathbf{B}_{zz} + \left(\sigma_{pre}\right)_{sz}\mathbf{B}_{sz}\, dV\right\}\mathbf{U} \\ &= -\lambda\,\delta\mathbf{U}^{\mathrm{T}}\mathbf{GU} \end{aligned} \tag{19}$$

where $\mathbf{G}$ is termed as the load-geometry matrix. By using Eqs. (11), (17) and (19), the governing equation for the discretized system is expressed as follows:

$$\begin{aligned} \delta\Pi_{total} &= \delta\Pi_{SE} + \delta\Pi_{buckling} \\ &= \int_V \delta\boldsymbol{\varepsilon}^T\mathbf{C}\boldsymbol{\varepsilon}dV - \lambda_{cr}\int_V \boldsymbol{\sigma}_{pre}{}^T\delta\boldsymbol{\varepsilon}'dV \\ &= \delta\mathbf{U}^T\mathbf{KU} - \lambda_{cr}\delta\mathbf{U}^T\mathbf{GU} \\ &= \delta\mathbf{U}^T\left(\mathbf{K} - \lambda_{cr}\mathbf{G}\right)\mathbf{U} \\ &= 0\,. \end{aligned} \tag{20}$$

Eq. (20) must be satisfied for arbitrary $\delta\mathbf{U}$ that satisfies the boundary condition. The resulting system equation for buckling analysis is finally given as:

$$\left(\mathbf{K} - \lambda_{cr}\mathbf{G}\right)\mathbf{U} = \mathbf{0}\,. \tag{21}$$

In order to obtain a nontrivial solution from Eq. (21), the determinant of the above equation must be zero:

$$\det\left(\mathbf{K} - \lambda_{cr}\mathbf{G}\right) = 0\,. \tag{22}$$

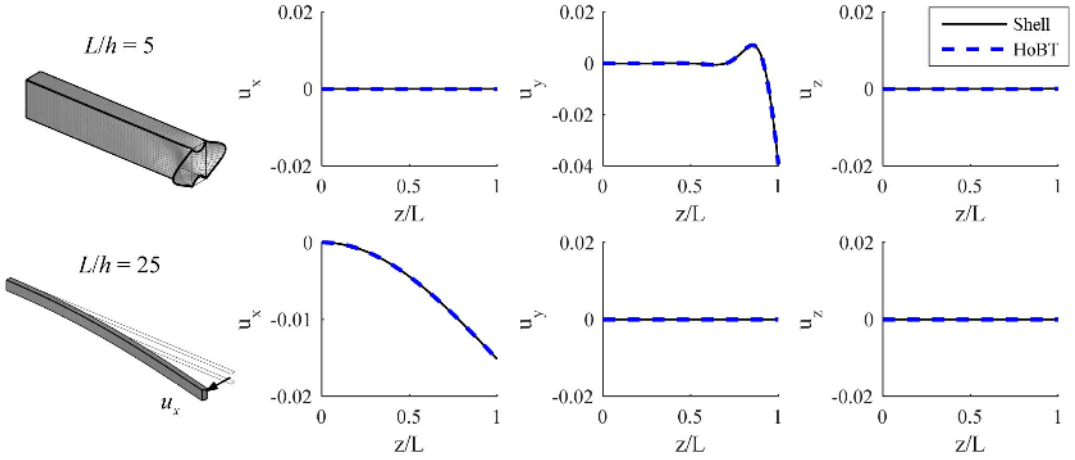

(a) Clamped-free condition with open end

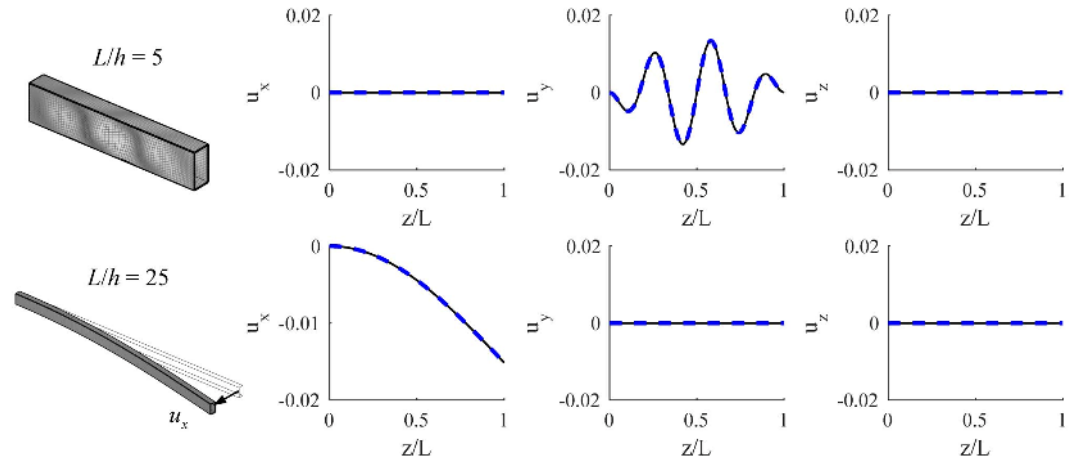

(b) Clamped-free condition with closed end

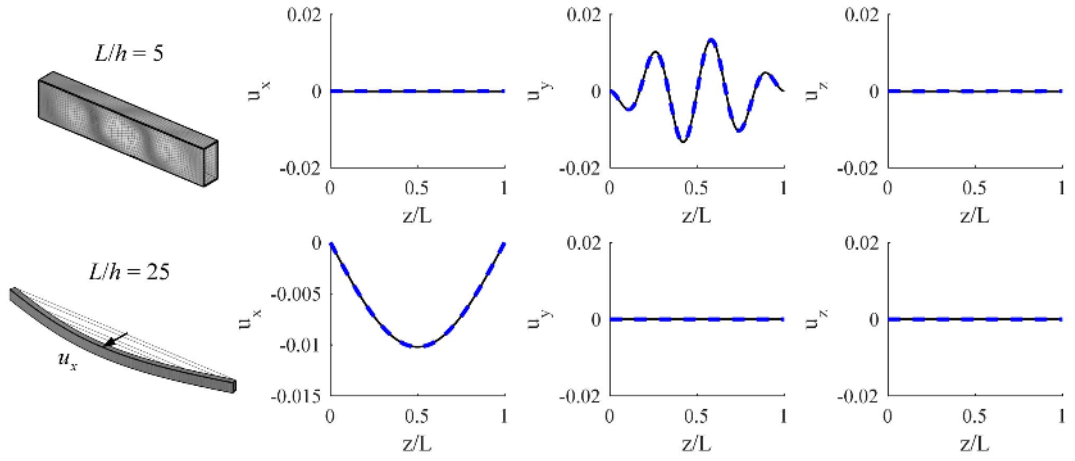

(c) Simply-supported condition with closed end

Fig. 4. Buckling mode shapes and 3-dimensional displacements plotted along the line of $x = 0$ and $y = h/2$ for varying z values for case study 1.

Subsequently, λ_{cr} is calculated by solving the eigenvalue problem (Eq. (21)), and its eigenvector represents the buckling pattern. The critical load is obtained by multiplying the prescribed load and λ_{cr} in Eq. (22).

5. Numerical examples

In this section, several case studies are performed by using Eq. (22). The results obtained by the present HoBT-based

buckling analysis are compared with those obtained by using the 8-node quadratic shell elements (S8R) in commercial software, ABAQUS.

5.1 Case study 1: Axial compressive loading

In case study 1, a buckling analysis of thin-walled beams under axial compressive loading is performed for different boundary conditions. With respect to the given boundary/loading conditions, a parametric study with variations in the dimensionless length, L / b, from 1 to 100 is performed to verify that the presented formulation works irrespective of beam length. The sectional dimension of the thin-walled beam is b = 0.06 m (width), h = 0.12 m (height), and t = 0.002 m (thickness). The material properties of the beam are given by Young's modulus E = 210 GPa and Poisson's ratio ν = 0.3. The prescribed unit load P_{pre} in Eq. (13) for axial compression is given by calculating Eq. (6) with $\mathbf{f}_{surf}$ defined as follows:

$$\left(f_{surf}\right)_z = \begin{cases} 1\ \left(\mathrm{N/m^2}\right) & (z=0) \\ -1\ \left(\mathrm{N/m^2}\right) & (z=L)\,. \end{cases} \tag{23}$$

Fig. 3 examines the effects of the boundary conditions including the clamped-free condition with open end (CFo), the clamped-free condition with closed end (CFc), and the simply-supported condition with closed ends (SSc). Here, a closed end refers to a beam end in which the sectional deformations such as warping and distortion are fully constrained. It can have only rigid-body motions. If the end is free to warp and distort, it is referred to as an open end. All box beams are subjected to axial compressive loading.

The results in Fig. 3 show that the results by the present HoBT formulation agree favorably with the shell finite element results for all boundary conditions considered. For instance, the averaged relative errors in the present results with respect to the shell results for the slenderness ratio L / h ranging from 1 to 100 are only 0.9 % and 0.1 %, respectively, for the CFo and CFc cases. Clearly, the transition points of L / h from the global to local buckling are accurately captured by the proposed HoBT method when compared with the shell analysis.

Fig. 4 sketches the deformed shapes for various L / h values and boundary conditions. Although the results by the shell analysis are not shown, the present deformed shapes agree well with those by the shell analysis. The figure also plots the three-dimensional displacements $\left(u_x, u_y, u_z\right)$ along the z-axis lying on $\left(x=0,\ y=h/2\right)$. Excellent agreements between the present HoBT and shell results are observed in the plots.

5.2 Case study 2: Torsional loading

In this case study, the buckling analysis for torsional loading is investigated in thin-walled box beams for various boundary conditions. The dimensions of the beam and the ranges of the slenderness ratio (L / h) are identical to those in case study 1. The same material properties as used in case study 1 are considered. The torsional loading is applied by constant shear stress $\mathbf{f}_{surf}$ on the cross-sections at both ends with the exception of the clamped point as:

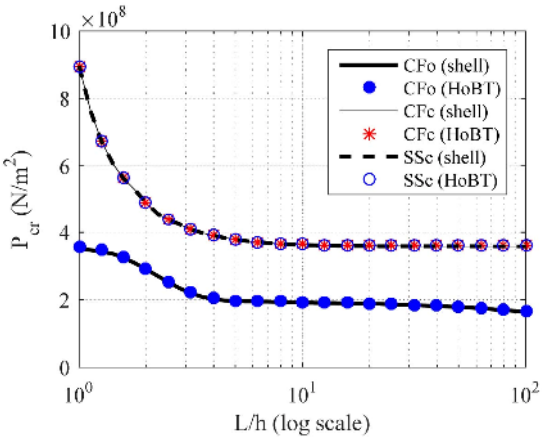

Fig. 5. The critical load (P_{cr}) for case study 2 (torsional loading case).

$$\left(f_{surf}\right)_s = \begin{cases} -1\ \left(\mathrm{N/m^2}\right) & (z=0) \\ 1\ \left(\mathrm{N/m^2}\right) & (z=L)\,. \end{cases} \tag{24}$$

The values of the critical load (P_{cr}) are plotted as a function of L / h for different boundary conditions in Fig. 5 and the buckling modes for some L / h values are sketched in Fig. 6. Excellent agreements between the results by the present HoBT-based formulation and those by the shell analysis (by ABAQUS) are apparent from Figs. 5 and 6.

In contrast to the axial buckling considered in case study 1, there is no distinct change in P_{cr} from local to global buckling in this case; compare Figs. 3 and 5. However, the local buckling with significant distortion occurs throughout the entire range of L / h considered, as may be observed from Fig. 6. This phenomenon is similar to that observed in the buckling of circular or polygonal tubes under torsional loading [41].

Figs. 5 and 6 also show that the CFc- and SSc-conditioned beams have exactly the same critical loads and buckling modes. Both of their buckling patterns can be characterized by local modes that do not involve $U_x, U_y, U_z, \theta_x, \theta_y$ and θ_z (rigid-body motions of the cross-section) everywhere throughout the beams due to their closed-end constraints. In case of the CFo-conditioned beams, no rigid-body motion of the cross-section occurs but significant cross-sectional deformations can occur due to the open-end condition.

It is not surprising that the buckling loads for the CFc-conditioned beams are larger than those for the CFo-conditioned beams; the cross-sectional constraint imposed on the beam at its end effectively reinforces the beam, as in case study 1.

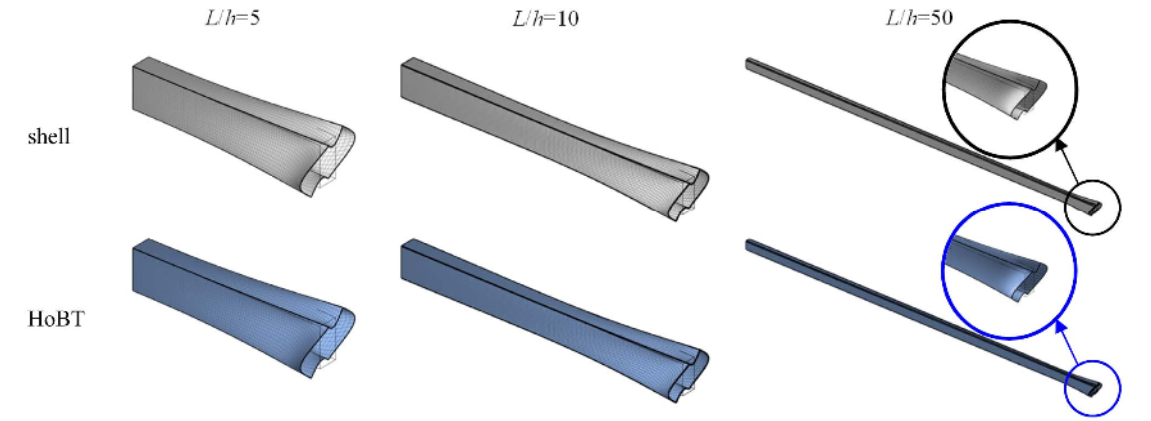

(a) Clamped-free condition with open end (CFo)

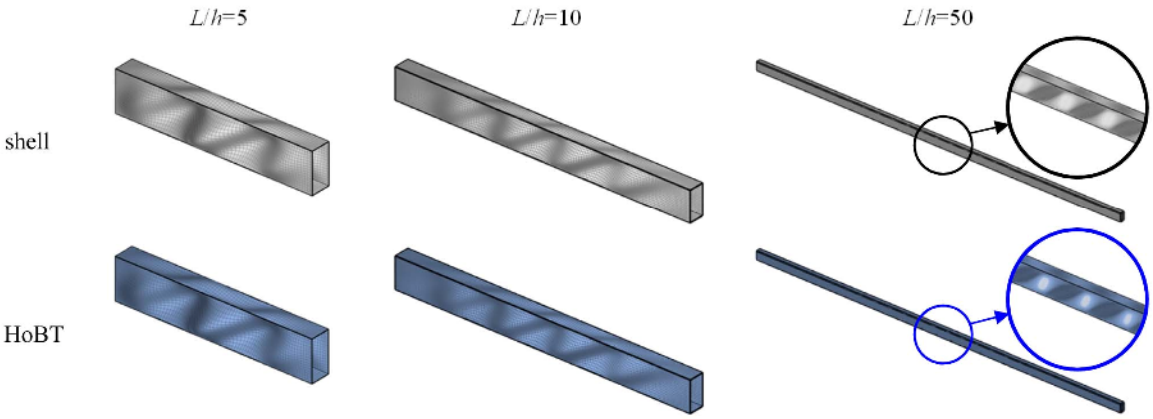

(b) Clamped-free condition with closed end (CFc)

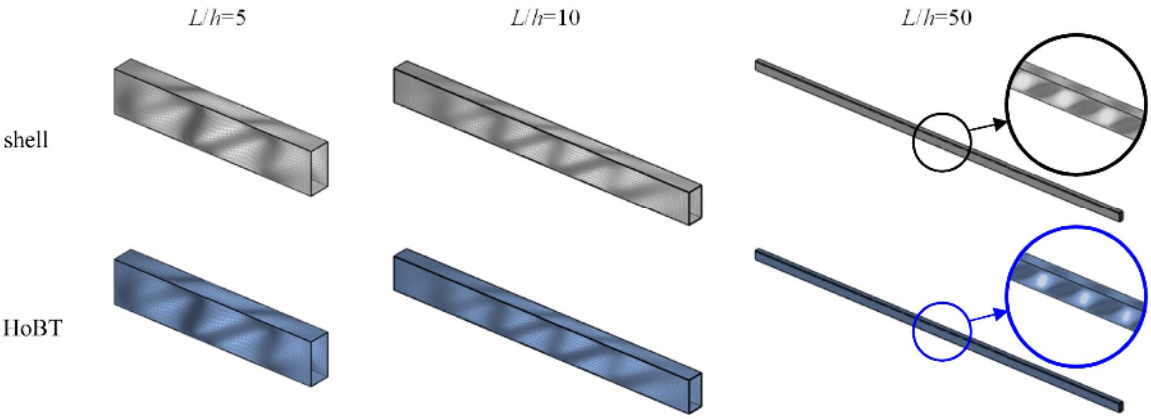

(c) Simply-supported condition with closed end (SSc)

Fig. 6. Buckling mode shapes for case study 2.

5.3 Case study 3: Bending loading

This case study considers thin-walled box beams under bending loads. The same geometry, material properties and slenderness ratios, as in the previous cases, are used. The numerical results are given in Fig. 7 for the critical loads and in Fig. 8 for the buckling mode shapes. The results by the present HoBT-based formulation agree very well with those by the shell (solid) finite elements (ABAQUS). The bending loading is applied as:

$$\left(f_{surf}\right)_z = \begin{cases} \dfrac{2}{h}\cdot y\ \left(\mathrm{N/m^2}\right) & \left(z=0\right) \\ -\dfrac{2}{h}\cdot y\ \left(\mathrm{N/m^2}\right) & \left(z=L\right). \end{cases} \tag{25}$$

A few remarks on the obtained results in Figs. 7 and 8 are worth making. Unlike in solid or thin-walled open beams exhibiting global lateral-torsional buckling when they are subjected to bending loading, thin-walled box beams under bending loading buckle in the local mode pattern involving cross-sectional deformations. In the CFo- and CFc-conditioned beams, global buckling can take place when L/h becomes larger than a certain value, which is about 40 and 50, respectively, in the present case. (See the buckling mode shapes for $L/h=80$).

As remarked in case study 2, the buckling behaviors of the CFc-conditioned and SSc-conditioned beams are virtually identical, but some difference is observed when $L/h>50$ as observed in the values of P_{cr} for the two beams. The main

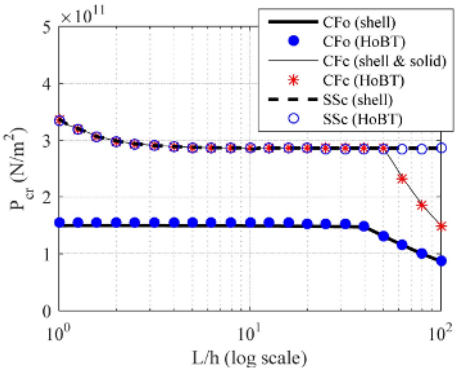

Fig. 7. The effects of the boundary condition on P_{cr} (critical load) for case study 3 (bending load case).

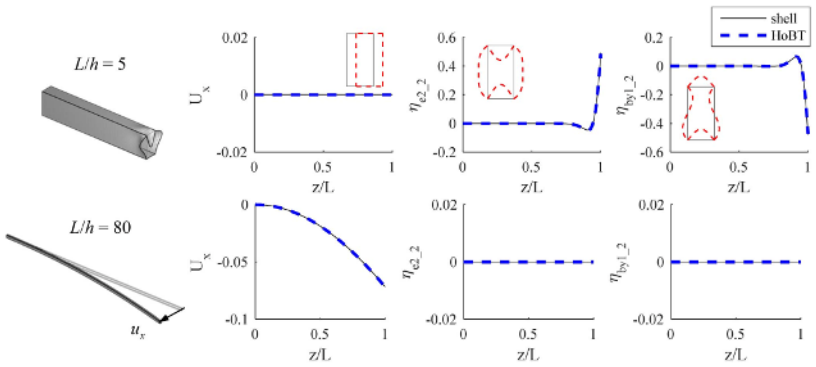

(a) Clamped-free condition with open end (CFo)

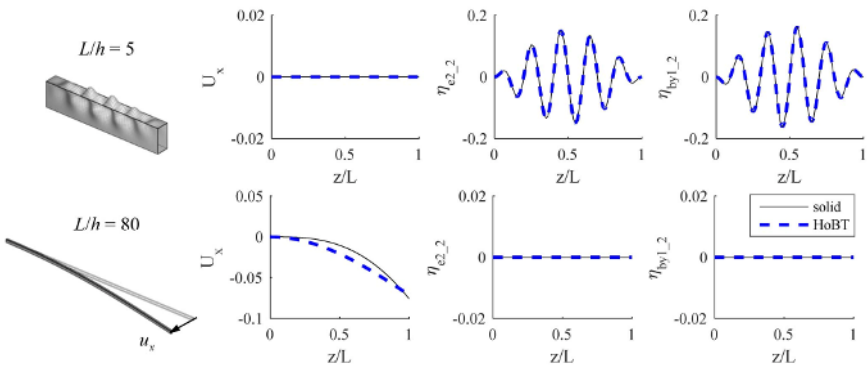

(b) Clamped-free condition with closed end (CFc)

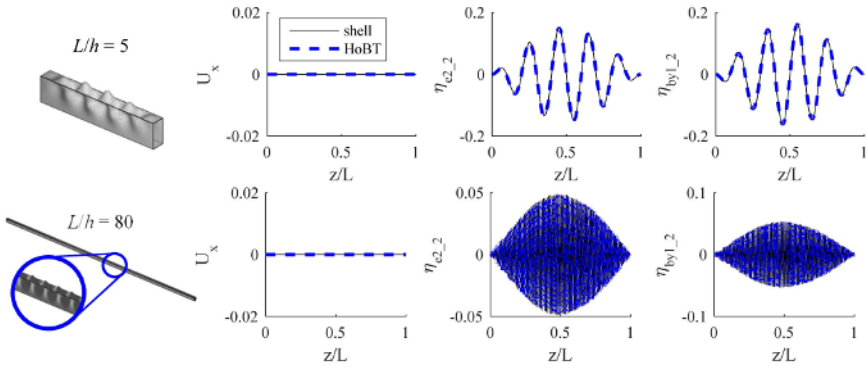

(c) Simply-supported condition with closed end (SSc)

Fig. 8. Buckling mode shapes and the axial variations of some field variables (U_x, η_{e2_2}, η_{by1_2}) for case study 3.

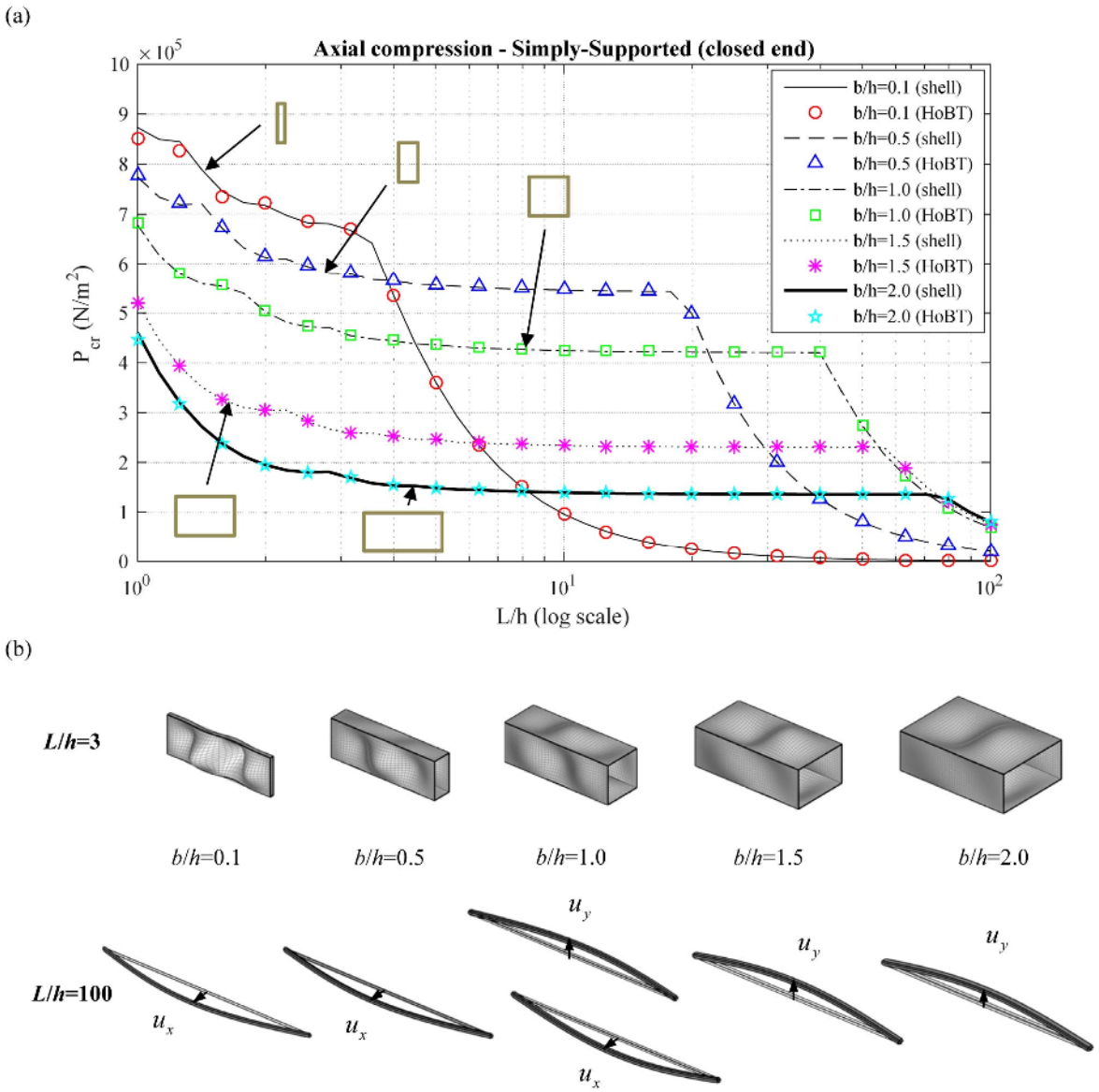

Fig. 9. The effects of b/h on P_{cr} considered in case study 4: (a) Critical load (P_{cr}); (b) buckling mode shapes.

reason is that the CFc-conditioned beams exhibit global buckling, decreasing the critical load (P_{cr}) while the SSc-conditioned beams buckle in the local buckling pattern; see Figs. 8(b) and (c) for $L/h = 80$. (For the CFc-conditioned beams with $L/h \geq 50$, the solid finite elements were used to obtain P_{cr} as the shell finite element calculations (ABAQUS) do not tend to yield consistent results).

5.4 Case study 4: Effects of b / h (aspect ratio) and t (thickness)

The goal to consider case study 4 is to investigate how accurately the present HoBT formulation predicts the critical load as compared with the shell finite element analysis for various values of b/h (the aspect ratio of the cross-section) and t (the wall thickness of the cross-section). The material properties and other geometric parameters are exactly the same as the CFo-conditioned and SSc-conditioned box beams subjected to axial compressive loading considered in case study 1. The results for various values of b/h with a fixed value of $h = 0.12$ m ($t = 0.002$ m) are presented in Fig. 9 for the SSc-conditioned beams and those for various values of t ($b = 0.06$ m, $h = 0.12$ m) are given in Fig. 10 for the CFo-conditioned beams.

As Figs. 9(a) and 10(a) show, the present HoBT-based formulation yields almost identical results to those obtained by the shell finite element analysis. This confirms that the present HoBT approach developed for buckling analysis of thin-walled box beams is uniformly valid for any values of b/h and t. The sudden transitions in the P_{cr} values observed in the plots of Figs. 9(a) and 10(a) describe accurately how the buckling patterns change from the local to global modes.

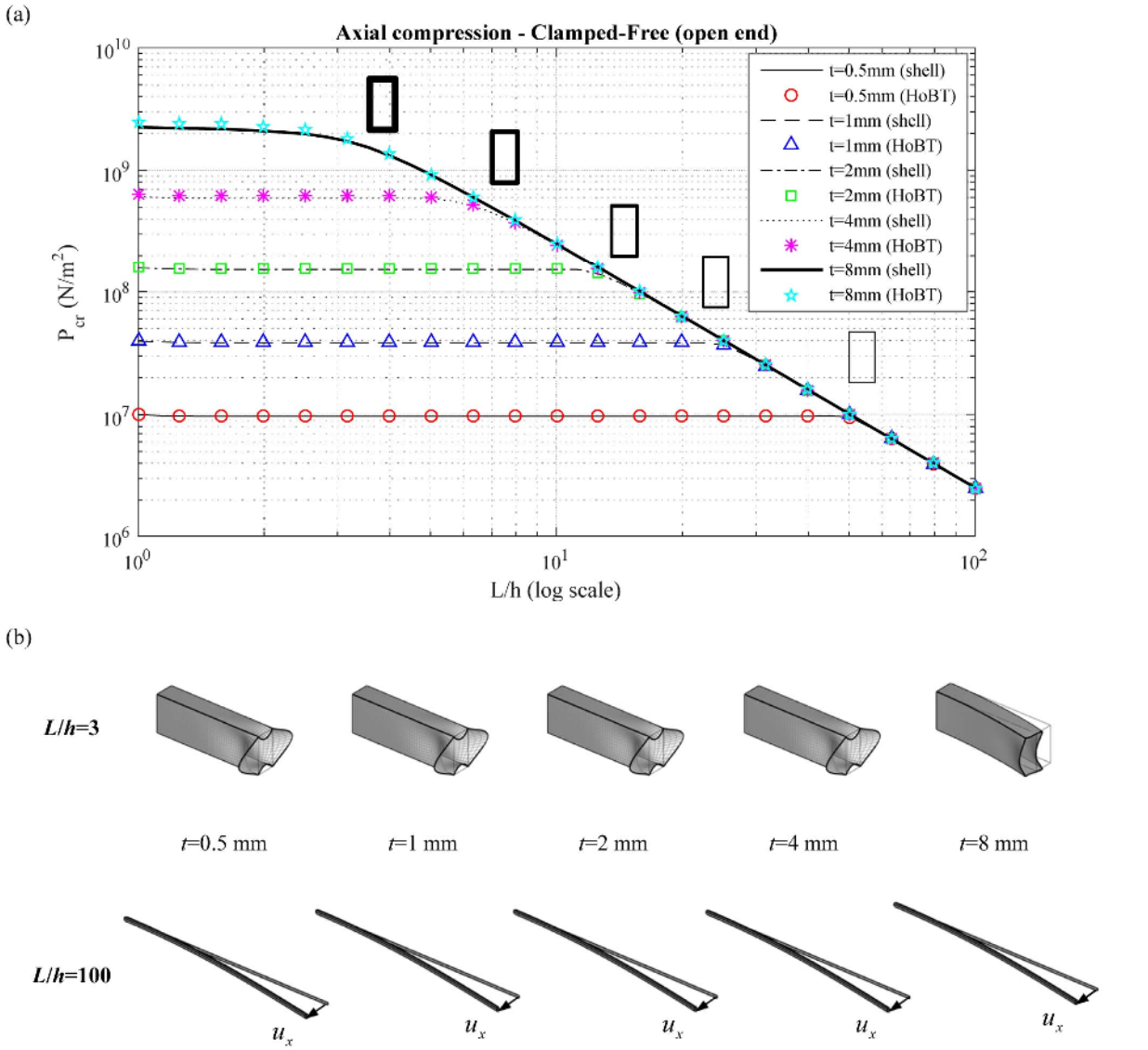

Fig. 10. The effect of t on P_{cr} considered in case study 4.

Their behaviors are accurately predicted by the proposed HoBT-based buckling analysis. Some representative buckling modes are sketched in Figs. 9(b) and 10(b).

5.5 Case study 5: Arbitrary loading

The objective to consider case study 5 is two-fold: checking the applicability of the proposed HoBT formulation to arbitrary loading cases and examining the effects of the number of the sets of the cross-sectional deformation modes on the obtained results. In this case, we consider two different loading conditions as:

Problem 1 (depicted in Fig. 11(a))
Applied loading:

$$\left(f_{surf}\right)_s = 1-\left(\frac{2}{h}\cdot s_1\right)^2 \left(\mathrm{N/m^2}\right) \qquad \left(\text{at } x=\frac{b}{2}, z=L\right). \quad (26)$$

Problem 2 (depicted in Fig. 12(a))
Applied loading:

$$\left(f_{surf}\right)_z = \begin{cases} 1\ \left(\mathrm{N/m^2}\right) & \left(-\frac{h}{4}\le y\le\frac{h}{4}; x=\frac{b}{2}, z=L\right) \\ -1\ \left(\mathrm{N/m^2}\right) & \left(-\frac{h}{4}\le y\le\frac{h}{4}; x=-\frac{b}{2}, z=L\right) \\ 0\ \left(\mathrm{N/m^2}\right) & \left(\text{otherwise}\right). \end{cases} \quad (27)$$

For both problems, the following geometry data and material properties are used:

$$b = 0.06 \text{ m}, h = 0.12 \text{ m}, t = 0.002 \text{ m}, L = 0.6 \text{ m}$$
$$E = 210 \text{ GPa}, \nu = 0.3.$$

The boundary conditions for both beams are clamped-free

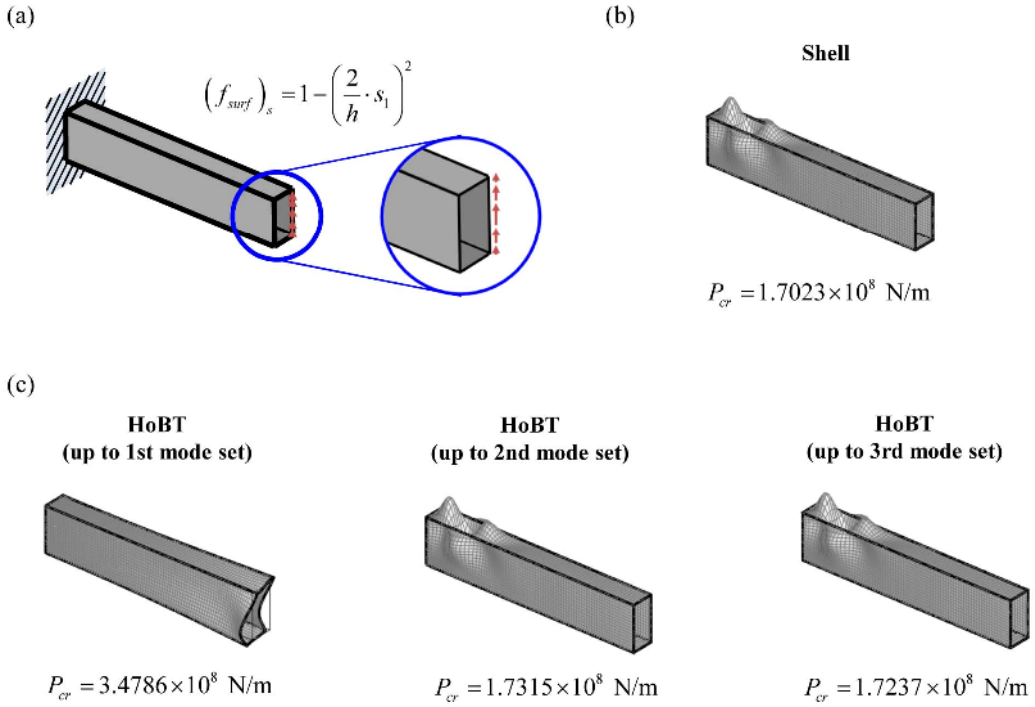

Fig. 11. The results for problem 1 of case study 5: (a) Loading and boundary conditions; (b) the results by shell finite element analysis; (c) the results by the present HoBT-based analysis.

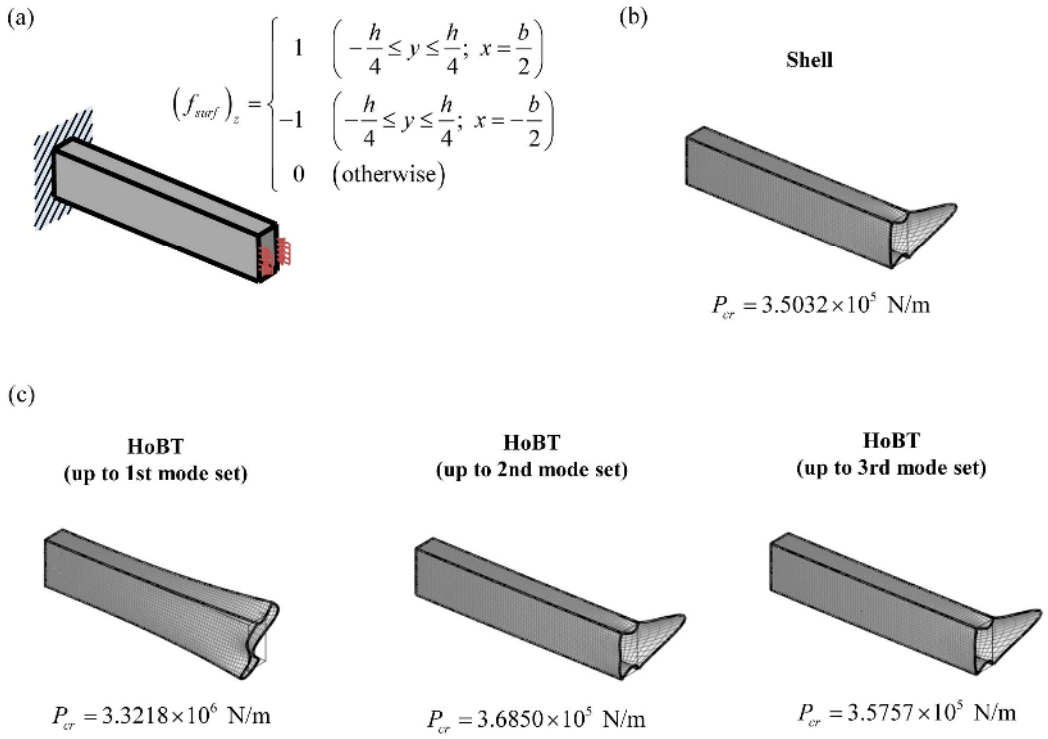

Fig. 12. The results for problem 2 of case study 5: (a) Loading and boundary conditions; (b) the results by shell finite element analysis; (c) the results by the present HoBT-based analysis.

with open end (CFo).

The critical loads and buckling modes obtained by the shell finite element calculations for Problems 1 and 2 are presented in Figs. 11(b) and 12(b), respectively. We present the HoBT-

based results by using different numbers of the cross-sectional mode sets. Referring to Table 1, we use the following notations in Figs. 11(c) and 12(c):

Representation	Included modes	Total DOFs
HoBT mode (up to 1st mode set)	($U_x, U_y, U_z, \theta_x, \theta_y, \theta_z$) and ($\chi_{e1}, W_{e1}, \cdots, \chi_{t1}, W_{t1}$)	6 + 12 = 18
HoBT mode (up to 2nd mode set)	All modes included in HoBT (up to 1st mode set) and ($\chi_{e2}, W_{e2}, \cdots, \eta_{t2\_2}$)	18 + 16 = 34
HoBT mode (up to 3rd mode set)	All modes included in HoBT (up to 2nd mode set) and ($\chi_{e3}, W_{e3}, \cdots, \eta_{t3\_2}$)	34 + 16 = 50.

The results in Figs. 11(c) and 12(c) show that the use of the first set of the cross-sectional deformation mode shapes along with the six rigid-body motions of the cross-section is not sufficient to yield accurate buckling loads or predict correct buckling modes. This is because highly-localized sectional deformation shapes, as observed in shell-based results in Figs. 11(b) and 12(b), cannot be correctly described only with the lowest cross-sectional mode set (and the rigid-body mode set). However, the use of HoBT including up to the 2nd cross-sectional mode set yields favorable results in comparison with the shell-based results.

The numerical calculations show that the predicted critical loads by the present HoBT-based formulations match the results by the shell finite element analysis only within 1.7 % (HoBT-up to 2nd mode set) and 1.3 % (HoBT-up to 3rd mode set) errors for problem 1. In case of problem 2, the errors are 5.2 % (HoBT-up to 2nd mode set) and 2.1 % (HoBT-up to 3rd mode set). The predicted buckling mode shapes by the present analysis virtually match those by the shell-based analysis. This example may justify the use of up to the 3rd cross-sectional mode set if highly accurate results by a beam-based analysis are desired.

6. Conclusions

In the study, beam-based buckling analysis was performed for thin-walled box beams for general beam boundary and loading conditions by using the higher-order beam theory (HoBT). In order to accurately capture the sectional deformation of a box beam, three sets of cross-sectional beam DOFs of the HoBT were employed in addition to the classical six DOFs representing the rigid-body motions of the beam cross-section. Then, the detailed finite element implementation procedure was presented to predict the critical loads and buckling modes.

The critical loads for various boundary and loading considered here were obtained within a maximum error of approximately 5 % if up to the 2nd cross-sectional mode set of the HoBT (34 DOFs) was used. The errors were reduced to less than 2 % when up to the 3rd cross-sectional mode set of the HoBT (50 DOFs) was used. The present HoBT-based buckling analysis was universally applied to the thin-walled box beams under arbitrary loading and boundary conditions. We expect that the present analysis can serve as a critical approach in performing buckling analysis of general box beam systems involving various joints.

Acknowledgments

This research was supported by a grant from the National Research Foundation of Korea (Grant No. 2014M3A6 B3063711, Grant No. 2016R1A5A1938472 and Grant No. 2016R1A2B3010231).

References

[1] P. Z. Qiao, J. F. Davalos and J. L. Wang, Local buckling of composite FRP shapes by discrete plate analysis, *Journal of Structural Engineering*, 127 (2001) 245-255.

[2] P. Qiao, F. Chen, J. Xu and Z. Lu, Local buckling analysis of restrained orthotropic plates under generic in-plane loading, *Journal of Engineering Mechanics*, 139 (2013) 936-951.

[3] L. P. Kollar, Local buckling of fiber reinforced plastic composite structural members with open and closed cross sections, *Journal of Structural Engineering*, 129 (2003) 1503-1513.

[4] G. J. Hancock, A. J. Davids, P. W. Key, S. C. W. Lau and K. J. R. Rasmussen, Recent developments in the buckling and nonlinear analysis of thin-walled structural members, *Thin-Walled Structures*, 9 (1990) 309-338.

[5] G. Yan-Lin, Local and overall interactive instability of thin-walled box-section columns, *Journal of Constructional Steel Research*, 22 (1992) 1-19.

[6] J. P. Papangelis and G. J. Hancock, Computer-analysis of thin-walled structural members, *Computers & Structures*, 56 (1995) 157-176.

[7] S. Sridharan and M. A. Ali, Interactive buckling in thin-walled beam-columns, *Journal of Engineering Mechanics*, 111 (1985) 1470-1486.

[8] S. Sridharan and M. A. Ali, An improved interactive buckling analysis of thin-walled columns having doubly symmetric sections, *International Journal of Solids and Structures*, 22 (1986) 429-443.

[9] Z. Kolakowski, Interactive buckling of thin-walled beams with open and closed cross-sections, *Thin-Walled Structures*, 15 (1993) 159-183.

[10] Z. Kolakowski and A. Teter, Interactive buckling of thin-walled closed elastic beams with intermediate stiffeners, *International Journal of Solids and Structures*, 32 (1995) 1501-1516.

[11] A. Manevich and Z. Kolakowski, Influence of local post-buckling behaviour on bending of thin-walled beams, *Thin-*

Walled Structures, 25 (1996) 219-230.

[12] K. Saade, B. Espion and G. Warzee, Non-uniform torsional behavior and stability of thin-walled elastic beams with arbitrary cross sections, *Thin-Walled Structures*, 42 (2004) 857-881.

[13] V. Vlasov, *Thin-walled Elastic Beams Israel Program for Scientific Translations*, Jerusalem, Israel (1961).

[14] R. Gonçalves and D. Camotim, GBT local and global buckling analysis of aluminium and stainless steel columns, *Computers & Structures*, 82 (2004) 1473-1484.

[15] P. Simao and L. S. da Silva, A unified energy formulation for the stability analysis of open and closed thin-walled members in the framework of the generalized beam theory, *Thin-Walled Structures*, 42 (2004) 1495-1517.

[16] R. Bebiano, N. Silvestre and D. Camotim, GBT formulation to analyze the buckling behavior of thin-walled members subjected to non-uniform bending, *International Journal of Structural Stability and Dynamics*, 7 (2007) 23-54.

[17] R. Gonçalves, P. Le Grognec and D. Camotim, GBT-based semi-analytical solutions for the plastic bifurcation of thin-walled members, *International Journal of Solids and Structures*, 47 (2010) 34-50.

[18] M. Casafont, F. Marimon, M. Pastor and M. Ferrer, Linear buckling analysis of thin-walled members combining the generalised beam theory and the finite element method, *Computers & Structures*, 89 (2011) 1982-2000.

[19] M. J. Andreassen and J. Jonsson, Distortional buckling modes of semi-discretized thin-walled columns, *Thin-Walled Structures*, 51 (2012) 53-63.

[20] A. Genoese, A. Genoese, A. Bilotta and G. Garcea, Buckling analysis through a generalized beam model including section distortions, *Thin-Walled Structures*, 85 (2014) 125-141.

[21] G. Garcea, L. Leonetti, D. Magisano, R. Gonçalves and D. Camotim, Deformation modes for the post-critical analysis of thin-walled compressed members by a Koiter semi-analytic approach, *International Journal of Solids and Structures*, 110-111 (2017) 367-384.

[22] R. F. Vieira, F. B. Virtuoso and E. B. R. Pereira, A higher order model for thin-walled structures with deformable cross-sections, *International Journal of Solids and Structures*, 51 (3-4) (2014) 575-598.

[23] R. F. Vieira, F. B. Virtuoso and E. B. R. Pereira, Buckling of thin-walled structures through a higher order beam model, *Computers & Structures*, 180 (2017) 104-116.

[24] E. Carrera, A. Pagani and J. R. Banerjee, Linearized buckling analysis of isotropic and composite beam-columns by Carrera unified formulation and dynamic stiffness method, *Mechanics of Advanced Materials and Structures*, 23 (9) (2016) 1092-1103.

[25] J. Jeong, J.-S. Kim, Y. J. Kang and M. Cho, A cross-sectional analysis of composite beams based on asymptotic framework, *Journal of Mechanical Science and Technology*, 26 (1) (2012) 161-172.

[26] N.-I. Kim, D. K. Shin and M.-Y. Kim, Improved flexural-torsional stability analysis of thin-walled composite beam and exact stiffness matrix, *International Journal of Mechanical Sciences*, 49 (2007) 950-969.

[27] W. Abramowicz, The effective crushing distance in axially compressed thin-walled metal columns, *International Journal of Impact Engineering*, 1 (3) (1983) 309-317.

[28] D. Kecman, Bending collapse of rectangular and square section tubes, *International Journal of Mechanical Sciences,* 25 (9-10) (1983) 623-636.

[29] C. Gui, J. Bai and W. Zuo, Simplified crashworthiness method of automotive frame for conceptual design, *Thin-Walled Structures*, 131 (2018) 324-335.

[30] J. Bai, G. Meng, H. Wu and W. Zuo, Bending collapse of dual rectangle thin-walled tubes for conceptual design, *Thin-Walled Structures*, 135 (2019) 185-195.

[31] F. Xu, X. Zhang and H. Zhang, A review on functionally graded structures and materials for energy absorption, *Engineering Structures*, 171 (2018) 309-325.

[32] F. Xu, S. Zhang, K. Wu and Z. Dong, Multi-response optimization design of tailor-welded blank (TWB) thin-walled structures using Taguchi-based gray relational analysis, *Thin-Walled Structures*, 131 (2018) 286-296.

[33] Y. Y. Kim and J. H. Kim, Thin-walled closed box beam element for static and dynamic analysis, *International Journal for Numerical Methods in Engineering*, 45 (1999) 473-490.

[34] Y. Y. Kim and Y. Kim, A one-dimensional theory of thin-walled curved rectangular box beams under torsion and out-of-plane bending, *International Journal for Numerical Methods in Engineering*, 53 (2002) 1675-1693.

[35] Y. Kim and Y. Y. Kim, Analysis of thin-walled curved box beam under in-plane flexure, *International Journal of Solids and Structures*, 40 (2003) 6111-6123.

[36] G. W. Jang and Y. Y. Kim, Theoretical analysis of coupled torsional, warping and distortional waves in a straight thin-walled box beam by higher-order beam theory, *Journal of Sound and Vibration*, 330 (2011) 3024-3039.

[37] G. W. Jang, S. M. Choi and Y. Y. Kim, Analysis of three thin-walled box beams connected at a joint under out-of-plane bending loads, *Journal of Engineering Mechanics*, 139 (2013) 1350-1361.

[38] S. Choi, Unified higher-order beam analysis for multiply-connected thin-walled box beams*, Ph.D. Thesis*, Mechanical Engineering, Seoul National University, Seoul, Korea (2016).

[39] I. Choi, G.-W. Jang, S. Choi, D. Shin and Y. Y. Kim, Higher order analysis of thin-walled beams with axially varying quadrilateral cross section, *Computers & Structures*, 179 (2017) 127-139.

[40] S. P. Timoshenko and J. M. Gere, *Theory of Elastic Stability*, McGrawHill-Kogakusha Ltd, Tokyo, Japan (1961).

[41] R. Gonçalves and D. Camotim, Buckling behaviour of thin-walled regular polygonal tubes subjected to bending or torsion, *Thin-Walled Structures*, 73 (2013) 185-197.

Yoon Young Kim received his B.S. and M.S. from Seoul National University and his Ph.D. from Stanford University in 1989. He has been on the Faculty of the School of Mechanical and Aerospace Engineering, Seoul National University since 1991. His research is focused on mechanics-based analysis and design including the mechanics of thin-walled beams.

Do-Min Kim received his B.S. and M.S. in Mechanical Engineering from Seoul National University, in 2011 and 2013. He is currently a doctoral candidate at the Division of WCU Multiscale Mechanical Design, School of Mechanical and Aerospace Engineering, Seoul National University. His research interest is buckling analysis of thin-walled beam structures based on the advanced beam theory.